

## CHAPTER 7

### SELECTIVE SOLAR ABSORBERS

*Peter Bermel,<sup>1,\*</sup> Jeongwon Lee,<sup>2</sup> John D. Joannopoulos,<sup>2</sup> Ivan Celanovic,<sup>2</sup> & Marin Soljačić<sup>2</sup>*

<sup>1</sup>Institute for Soldier Nanotechnologies, 77 Massachusetts Avenue, Cambridge, Massachusetts 02139

<sup>2</sup>Birck Nanotechnology Center, Electrical & Computer Engineering, 1205 W. State St., West Lafayette, Indiana

\*Address all correspondence to Peter Bermel E-mail: pbermel@purdue.edu

*Efficiently capturing sunlight as heat is useful for a variety of applications, such as solar heating, solar thermal electricity generation, solar thermoelectrics, and solar thermophotovoltaics. This process is most efficient when selective solar absorbers can be used to absorb most of the solar wavelengths found at the earth's surface under standard atmospheric conditions, while suppressing infrared re-radiation induced by heating of the selective absorber. In practical terms, this generally corresponds to absorbing short wavelengths up to a certain cutoff wavelength, and reflecting everything else. There are six classes of selective solar absorbers reviewed here: intrinsic absorbers, semiconductor–metal tandems, multilayer tandems, ceramic–metal composites (known as cermets), textured absorbers, and photonic crystals. It is found that the performance of cermets is the highest of the simple structures, while photonic crystals have the most room for improvement in the future, owing to unique capabilities in terms of selectivity with respect to wavelength, angle, and polarization.*

## 1. INTRODUCTION

Many technologies require the ability to extract heat from an appropriate source(s) and to direct it where it is needed, either for direct use or for conversion into electricity. One almost universally available heat source for terrestrial applications is sunlight. The sun supplies approximately 10,000 quads (3 quadrillion kW/h) of energy to the surface of the earth every day; as of 2004, global primary energy production was approximately 1.22 quads a day, or about 0.012% of the energy delivered to the surface of the earth.<sup>1</sup> While highly absorptive surfaces in the visible and infrared (IR) are readily available, efficiently capturing sunlight as heat is complicated by the problem of thermal re-radiation.<sup>2–6</sup> In particular, a blackbody emitter illuminated by the unconcentrated standard AM1.5 solar spectrum with a solar constant of 1 kW/m<sup>2</sup> will reach thermal equilibrium at a temperature of 115°C, assuming an ambient temperature of 25°C, and no conductive or convective losses. Thus, applications such as thermoelectrics that work more efficiently at temperatures higher than 115°C require either solar optical concentration and/or selective solar absorbers. The advantage of pursuing the latter approach exclusively is that it allows for higher equilibrium temperatures without increasing the losses and complexity of the solar thermal energy system.

### NOMENCLATURE

$B$	solar concentrator window transmissivity	$T_c$	temperature of the cold heat sink (K)
$C$	optical solar concentration	<b>Greek Symbols</b>	
$dI/d\lambda$	solar intensity per unit wavelength ( $\text{W/m}^{-2}\text{nm}^{-1}$ )	$\bar{\alpha}$	spectrally averaged absorptivity
$f$	metal volume fraction (in cermets)	$\bar{\epsilon}$	spectrally averaged emissivity
$I_s$	solar intensity ( $\text{W/m}^{-2}$ )	$\eta_c$	Carnot efficiency
$T$	system temperature (K)	$\eta_t$	thermal transfer efficiency
$T_h$	temperature of the initial heat input (K)	$\lambda$	wavelength (nm)
		$\sigma$	Stefan–Boltzmann constant ( $\text{W/m}^{-2}\text{K}^{-4}$ )

Selective solar surfaces function by discriminating between the wavelengths containing most of the incoming solar energy and the wavelengths carrying most of the blackbody radiation for a device at the designated operating temperature. It is well known from Planck's law of blackbody radiation that the peak wavelength of a blackbody spectrum scales inversely with temperature. Since the sun's surface can be considered to be at a temperature of approximately 5500°C, and any realistic terrestrial application will involve much lower temperatures than that, a significant gap opens up between the regimes in which high and low absorptivity and emissivity are needed. If we restrict ourselves to a short-wavelength regime with unit emissivity and a long-wavelength regime with zero emissivity, the ideal wavelength at which such a transition between the two should occur will depend on the exact operating temperature and solar optical concentration employed. For example, a selective solar absorber in unconcentrated sunlight operating at 400°C with a perfect sharp ideal cutoff wavelength of 1.775  $\mu\text{m}$  will capture 92.8% of incoming sunlight as heat (assuming no other losses).

The fraction of sunlight captured as heat at a particular temperature  $T$  and solar optical concentration  $C$  can be defined as the thermal transfer efficiency  $\eta_t$ , and can be written as<sup>4</sup>

$$\eta_t = B\bar{\alpha} - \frac{\bar{\epsilon}\sigma T^4}{CI_s} \quad (1)$$

where  $B$  is the window transmissivity (if present),  $\bar{\alpha}$  is the spectrally averaged absorptivity,  $\bar{\epsilon}$  is the spectrally averaged emissivity,  $\sigma$  is the Stefan–Boltzmann constant, and  $I_s$  is the solar intensity, generally taken as 1  $\text{kW/m}^2$ . The spectrally averaged absorptivity can be written as<sup>4</sup>

$$\bar{\alpha} = \frac{1}{I_s} \int_0^\infty d\lambda \bar{\epsilon}(\lambda) \frac{dI}{d\lambda} \quad (2)$$

where  $dI/d\lambda$  is the solar intensity per unit wavelength. The spectrally averaged emissivity can be written as<sup>4</sup>

$$\bar{\epsilon} = \frac{1}{\sigma T^4} \int_0^\infty d\lambda \frac{\epsilon(\lambda)}{\lambda^5 [\exp(hc/\lambda kT) - 1]} \quad (3)$$

It is apparent that both absorptivity and emissivity are closely linked, in that the emissivity spectrum of the absorber affects both quantities. The two can be combined as follows:<sup>4</sup>

$$\eta_t = \frac{1}{CI_s} \int_0^\infty d\lambda \epsilon(\lambda) \left\{ BC \frac{dI}{d\lambda} \frac{2\pi hc^2}{\lambda^5 [\exp(hc/\lambda kT) - 1]} \right\} \quad (4)$$

In this form, it is clear that for every wavelength, the quantity in curly braces in the above equation will be either positive or not. For positive values, we would like the emissivity to be as large as possible (i.e., 1), while for negative values, we would like the emissivity to be as small as possible (i.e., 0). Typically, this corresponds to a step function in emissivity from 1 to 0 at a cutoff wavelength that falls somewhere in the solar spectrum. Figure 1 shows the optimal emissivity as a function of wavelength superimposed on the AM1.5 solar spectrum for an exemplary concentration of 100 suns, held at 1000 K. Only wavelengths where the power of concentrated sunlight exceeds the emission of a blackbody at 1000 K are fully absorbed; the remaining wavelengths are reflected back into space.

In Fig. 2, we show the optimal cutoff wavelength as a function of the operating temperature and solar concentration. A distinct trend becomes apparent, where higher concentrations and lower operating temperatures lead to longer wavelength cutoffs, while the opposite conditions lead to shorter wavelength cutoffs. Along similar lines, Fig. 3 shows the thermal transfer efficiency as a function of operating temperature and solar optical concentration. A similar trend also emerges here, in that higher concentrations and lower operating temperatures lead to high thermal transfer efficiencies, and the opposite conditions lead to much lower thermal transfer efficiencies—all the way down to 0%.

On the other hand, the maximum conversion efficiency possible for any system converting thermal energy into electricity is the so-called Carnot efficiency,  $\eta_c$ , given by

$$\eta_c = 1 - T_c/T_h \quad (5)$$

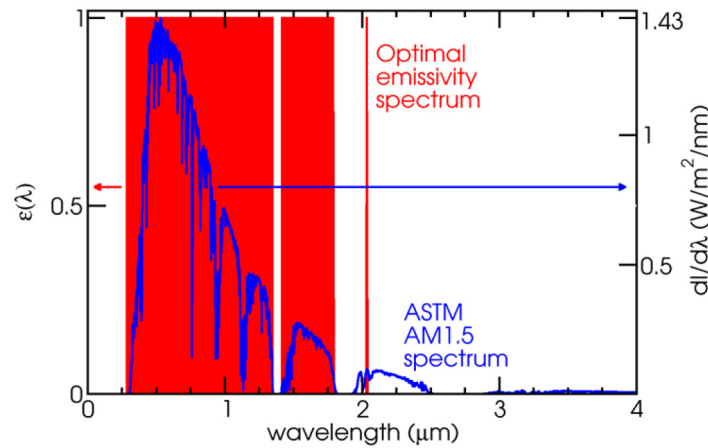


**FIG. 1:** The standard AM1.5 solar spectrum (blue) and optimal emissivity spectrum for a selective solar absorber subject to a concentration of 100 suns, operating at 1000 K (red). Only wavelengths with concentrated solar energy exceeding the emission of a blackbody at 1000 K are absorbed; the rest are completely reflected.

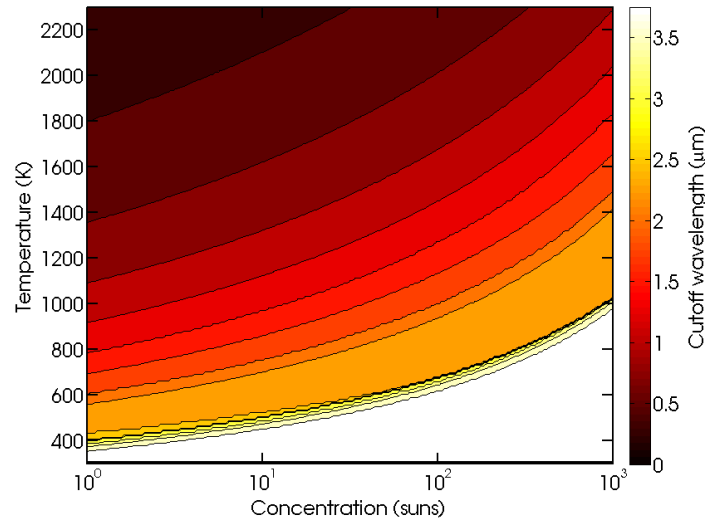


**FIG. 2:** Optimal cutoff wavelength (in  $\mu\text{m}$ ) for an ideal selective solar absorber as a function of solar optical concentration ( $x$  axis, plotted on a logarithmic scale) and temperature ( $y$  axis). Contour lines are equidistant in wavelength.

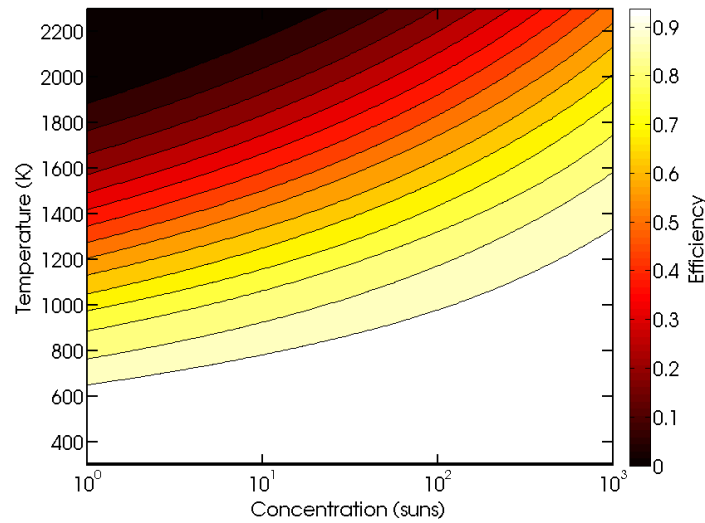


**FIG. 3:** Thermal transfer efficiency for an ideal selective solar absorber as a function of solar optical concentration ( $x$  axis, plotted on a logarithmic scale) and temperature ( $y$  axis). Contour lines are equidistant in efficiency.

where  $T_h$  is the temperature of the initial heat input, while  $T_c$  is the temperature of the cold heat sink. Thus, there is an inherent tension between efficiently harvesting sunlight as heat and efficiently converting that heat to electricity. As a result, a system-level approach is often required to maximize the performance of the overall energy conversion process. Such an analysis has been explored in recent literature.<sup>2–6</sup>

## 2. OVERVIEW OF SELECTIVE SOLAR ABSORBERS

As illustrated in the previous section, selective absorbers function best by absorbing wavelengths with high concentrations of solar power, but reflecting wavelengths with high amounts of blackbody radiation at their operating temperature. Ideally, they can also be manufactured at low cost and exhibit long-term stability under chemical, physical, and thermal stress associated with their projected operating conditions.

Six representative types of selective solar absorbers are shown in Fig. 4. Intrinsic absorbers are homogeneous materials possessing some inherent spectral selectivity, induced by dielectric dispersion as a function of wavelength. In general, they are structurally stable and easy to fabricate, but offer less-than-ideal spectral selectivity. In semiconductor–metal tandem structures, as shown in Fig. 4(b), semiconductor layers absorb short-wavelength radiation and metal layers suppress thermal emission in the IR range. Semiconductor materials suitable for this approach include Si, Ge, and PbS. Anti-reflection (AR) coatings are usually deposited on top to reduce reflectance loss originating from the high refractive index of the semiconductor materials. Figure 4(c) illustrates how multilayer absorbers consist of alternating layers of metal and dielectric. Metal layers effectively reduce the reflectance in the IR region, and dielectric layers increase the absorption in the visible region. Metal–dielectric composites, or cermets, shown in Fig. 4(d), consist of fine metal particles in a dielectric or ceramic matrix. Cermets show good selectivity at high temperature and have been successfully commercialized. Absorbers based on surface texturing illustrated in Fig. 4(e) effectively trap and absorb short-wavelength radiation while reflecting long-wavelength IR thermal radiation. The microstructure of the surface, such as the orientation and mean feature height, controls the degree of selectivity.<sup>5</sup> Finally, due to recent advances in the semiconductor processing technology, the fabrication of nanostructures with wavelength-scale features, known as photonic crystals (PhCs), has become possible. These PhC-based designs, illustrated schematically in Fig. 4(f), allow for unprecedented control over the spectral and angular selectivity of the devices, compared to all the previous candidates.

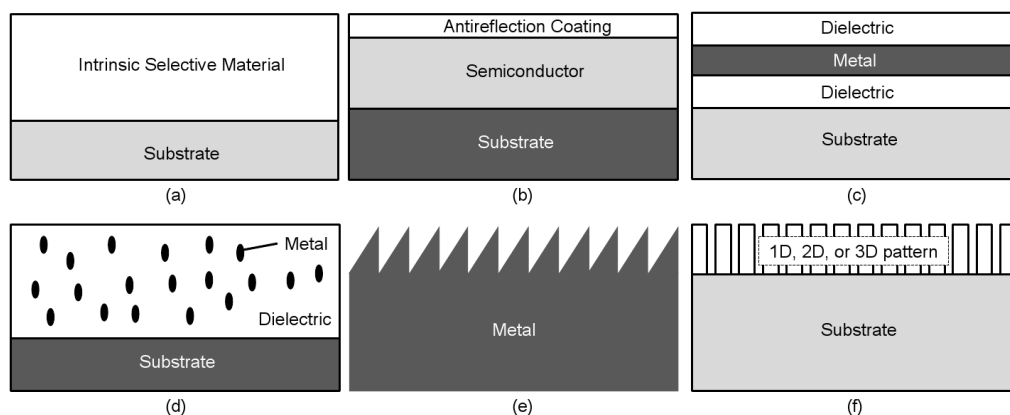


**FIG. 4:** Schematic designs of the six types of selective solar absorbers (adapted from Ref. 5): (a) intrinsic absorbers, (b) semiconductor-metal tandems, (c) multilayer absorbers, (d) cermets (metal-dielectric composites), (e) surface texturing, and (f) PhC-based designs.

### 3. STATE OF THE ART SELECTIVE SOLAR ABSORBERS

#### 3.1 Intrinsic Absorbers

Intrinsic solar selective properties are found in transition metals and semiconductors, but no natural materials have perfect ideal selectivity.<sup>6</sup> They also need structural or compositional modifications to be useful. Metals generally possess a plasmon frequency, above which absorptivity gradually increases. However, the plasmon frequency of a typical metal is well into the ultraviolet, as shown in Fig. 5(a)—well above the ideal cutoff wavelength for reasonable operating conditions. In a few cases, such as tungsten, interband crossings can provide additional absorptivity in the visible and near-IR, as shown in Fig. 5(b). How-

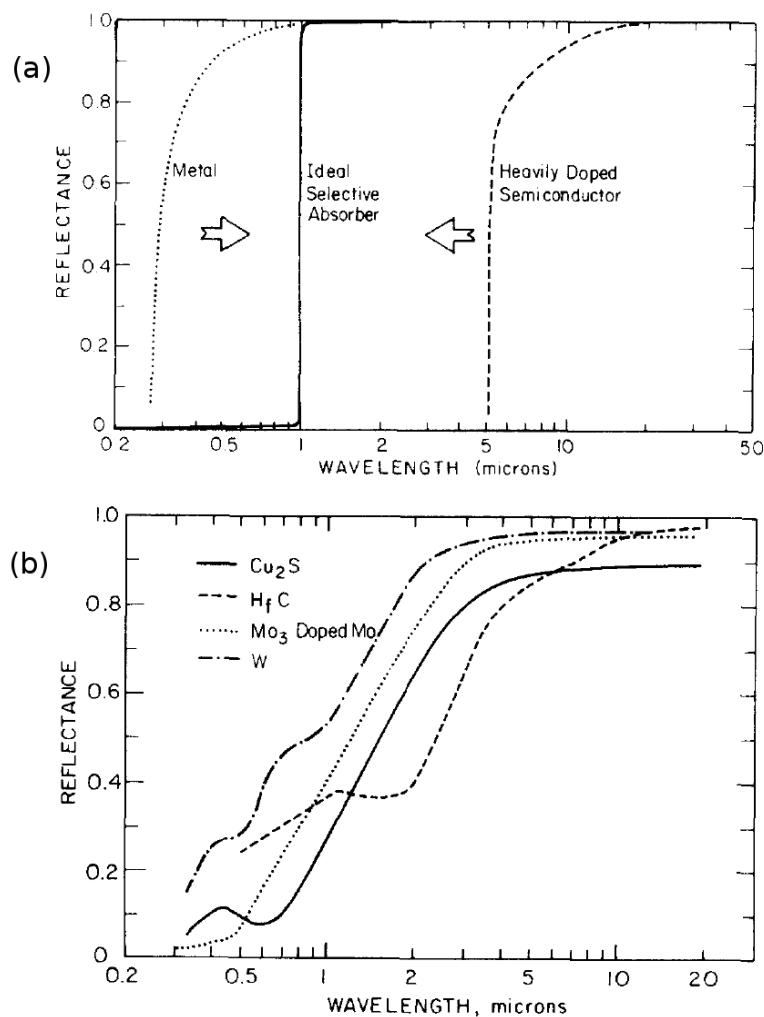


**FIG. 5:** (a) Reflectance of an ideal selective absorber compared to that of a metal and a heavily doped semiconductor. (b) Spectral reflectance for the intrinsic materials HfC, tungsten, MoO<sub>3</sub>-doped Mo, and Cu<sub>2</sub>S (adapted from Ref. 6).

ever, tungsten's intrinsic selectivity is still far from ideal. Alternatively, degrading the conductivity of the sample via scattering centers can help shift the plasmon frequency down into the IR, as in the case of  $\text{MoO}_3$ -doped Mo, shown in Fig. 5(b). Also, unusually conductive compound materials, such as  $\text{ZrB}_2$ , can exhibit a plasmon frequency that roughly matches the ideal cutoff wavelength. In conjunction with a  $\text{Si}_3\text{N}_4$  AR layer,  $\text{ZrB}_2$  has been measured to display spectrally averaged absorptivity of  $\bar{\alpha} = 0.93$  and spectrally averaged emissivity of  $\bar{\epsilon} = 0.09$  at 375 K; it can also survive in air up to temperatures of 800 K.<sup>7</sup> Highly degenerate semiconductors such as  $\text{Cu}_2\text{S}$  also show some solar selectivity, but require additional features to achieve acceptable performance. In general, they function best as primary layers for more complex selective absorber designs, such as multilayer stacks or cermet.

### 3.2 Semiconductor–Metal Tandems

Semiconductor materials are generally transparent for frequencies below their electronic band gap, but absorb strongly for higher frequencies. If a semiconductor is placed on a metal, short-wavelength solar radiation in the visible region will be absorbed by the semiconductor layer, while long-wavelength radiation will pass through the semiconductor and get reflected back by the metal layer,<sup>6</sup> as is illustrated in Fig. 6. Depending on the operating conditions, a wide variety of semiconductors may be suitable for selective solar absorbers, including silicon, germanium, and lead sulfide. Due to the high refractive index found near the band edge of most semiconductors, which creates unwanted reflection for frequencies above the band gap, an AR coating is generally added to suppress reflection and, thus, enhance performance.

Donnadieu et al.<sup>8</sup> considered a silicon/germanium tandem absorber placed on a silver reflector with an AR coating in front, consisting of four layers of transparent dielectrics with refractive indices varying from 1.43 to 2.79. Optimization via simulation yielded spectrally averaged absorptivity of  $\bar{\alpha} = 0.89$  and spectrally averaged emissivity of  $\bar{\epsilon} = 0.0389$  at 300°C and  $\bar{\epsilon} = 0.0545$  at 500°C.<sup>8</sup> Okuyama et al.<sup>9</sup> used an amorphous silicon absorber with an aluminum reflector and an AR coating consisting of  $\text{SiO}_2/\text{TiO}_2$ . This selective absorber had  $\bar{\alpha} = 0.79\text{--}0.81$  and  $\bar{\epsilon} = 0.12\text{--}0.14$  at 400°C.<sup>9</sup> More recently, Bermel

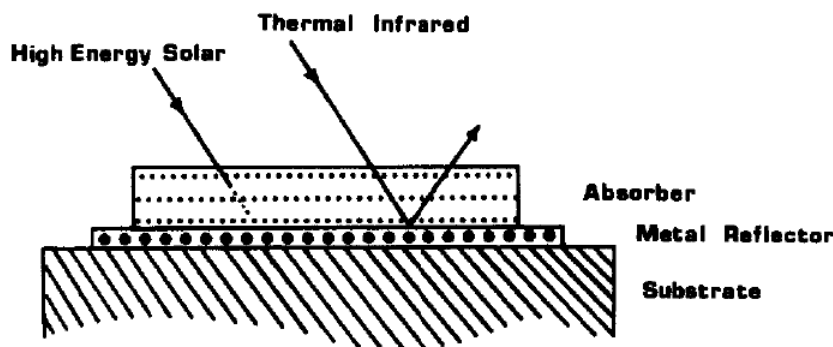


**FIG. 6:** Schematic cross section of a semiconductor-metal tandem selective absorber (adapted from Ref. 6).

et al.<sup>4</sup> numerically optimized a large class of selective solar absorbers under two sets of conditions. For unconcentrated sunlight ( $C = 1$ ) at an absorber temperature  $T = 400$  K, a germanium absorber and silver reflector with optimized front and back coatings showed  $\bar{\alpha} = 0.907$  and  $\bar{\epsilon} = 0.016$  at 400 K (Fig. 7), with a thermal transfer efficiency of 0.881. For concentrated sunlight ( $C = 100$ ) at an absorber temperature  $T = 1000$  K, silicon actually has an appropriate band gap. Combining hot silicon at 1000 K with a silver back reflector and multilayer front and back coatings yields  $\bar{\alpha} = 0.868$  and  $\bar{\epsilon} = 0.073$ , for a thermal transfer efficiency of 0.822. The slightly lower efficiency at 1000 K can be attributed to the greater overlap between the spectrum of a blackbody emission at 1000 K and the sun.<sup>4</sup>

### 3.3 Multilayer Absorbers

Multilayer thin films, or interference stacks, consist of alternating dielectric and metal layers, as shown in Fig. 8(a), where metal layers of less than one skin depth (e.g., several nanometers) allow for partial transparency.<sup>6</sup> A particular range of wavelengths of incident solar energy can experience enhanced absorption caused by multiple reflections at layer interfaces. To understand the effect of multiple reflections, the emission spectrum of each layer was analyzed by Narayanaswamy and Chen,<sup>10</sup> under the assumption that only one layer participates in the emission, while the rest of the films act as filters. The multilayer absorber model consisted of 11 unit cells with 10 nm of silver and 150 nm of vacuum. Figure 8(b) shows the emission spectra of the fifth and tenth layers calculated at room temperature. Compared to a bare 10-nm silver film, emissivity is predicted to decrease by two orders of magnitude in the IR. Even though the emissivity in the visible range is not high enough to be a good selective absorber, and it is very challenging to fabricate this structure, it demonstrates the basic concept that this simple multilayer structure can profoundly modify optical properties.<sup>10</sup>

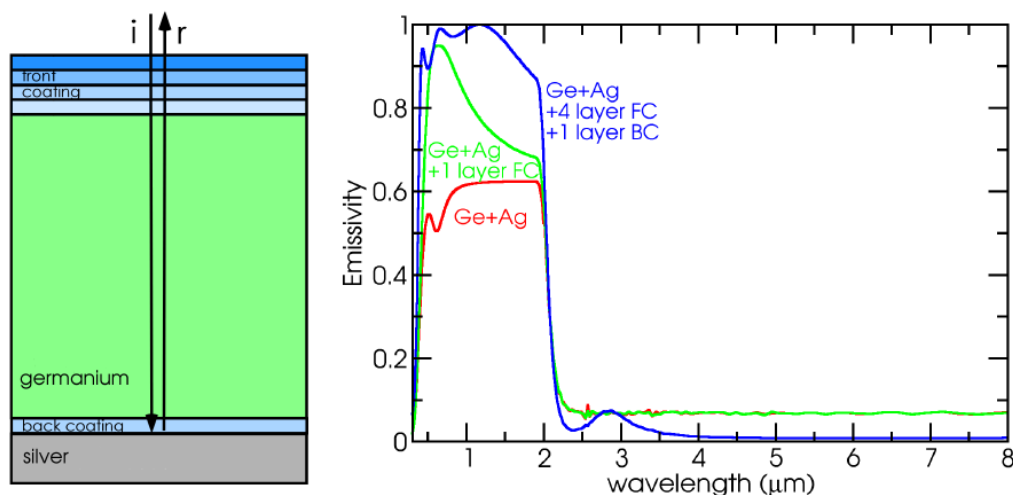


**FIG. 7:** (a) Schematics of the Ge/Ag selective solar absorber with optimized front and back coatings (optimized to work in unconcentrated sunlight at absorber temperature 400 K) and (b) simulated emittance spectra of (a) (adapted from Ref. 4).



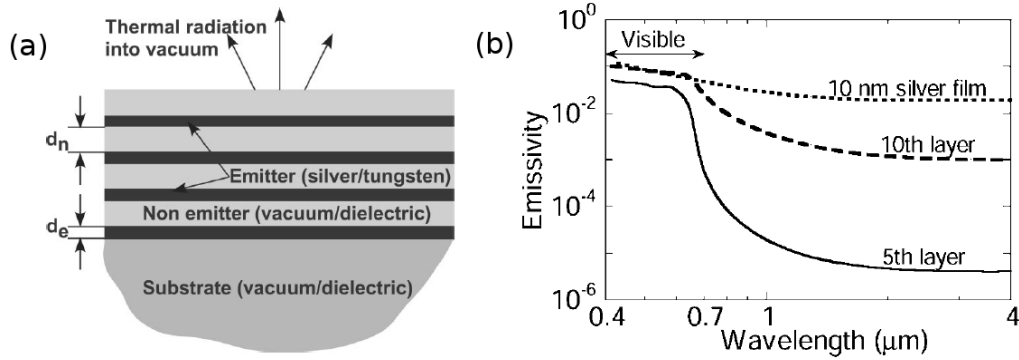


**FIG. 8:** (a) Schematic of a multilayer absorber. Each unit cell consists of a metal and a dielectric layers. (b) Emission spectrum of an 11-period multilayer absorber consisting of 10 nm of silver and 150 nm of vacuum. The tenth layer has one film above and nine films below it, and fifth film has five films on either side (adapted from Ref. 10).

Narayanaswamy et al.<sup>11</sup> analyzed thermal emission from periodic alternating layers of tungsten (W) and alumina ( $\text{Al}_2\text{O}_3$ ). This structure is easier to fabricate than structures with two-dimensional (2D) or three-dimensional (3D) periodicity, and exhibits fairly good wavelength selectivity, as shown in Fig. 9.<sup>10,11</sup> Unfortunately, the spectrally averaged absorptivity, emissivity, and thermal transfer efficiency for this design were not provided in Refs. 10 and 11.

Li et al.<sup>13</sup> optimized and fabricated the following aperiodic multilayer absorber structure:  $\text{SiO}_2(105 \text{ nm})/\text{Ti}(15 \text{ nm})/\text{SiO}_2(95 \text{ nm})/\text{Al}(\geq 100 \text{ nm})$ . It showed average absorptivity over 0.95 in the visible at normal incidence and over 0.90 up to an incident angle of  $60^\circ$ . It also displayed relatively low spectrally averaged emissivity of 0.063 for normal incidence at 600 K, as shown in Fig. 10.<sup>13</sup>

Sergeant et al.<sup>14</sup> calculated the spectral performance of a planar aperiodic multilayer absorber for high-temperature applications. For 720 K, the optimized structure composed

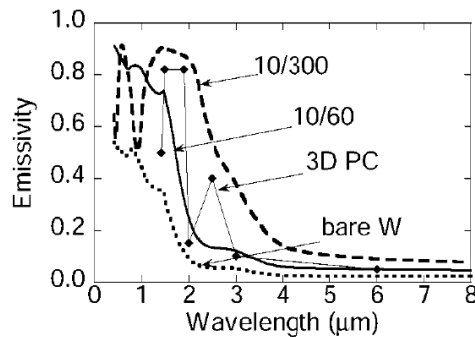


**FIG. 9:** Emission spectrum of the  $\text{W}/\text{Al}_2\text{O}_3$  periodic multilayer absorbers. The curves marked 10/60 and 10/300 refer to 10 nm of W and 60 nm of  $\text{Al}_2\text{O}_3$  and 10 nm of W and 300 nm of  $\text{Al}_2\text{O}_3$ , respectively. Both absorbers consist of 10 unit cells. 3D PC refers to the experimental data from Refs. 10 and 12.

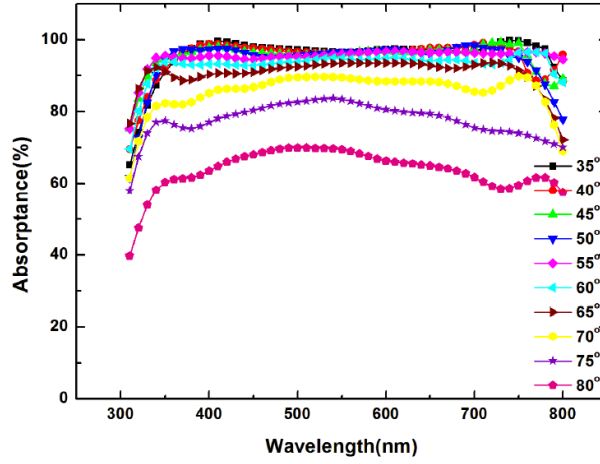


**FIG. 10:** Measured absorbance with incident angles for the structure of  $\text{SiO}_2(105 \text{ nm})/\text{Ti}(15 \text{ nm})/\text{SiO}_2(95 \text{ nm})/\text{Al}(0.100 \text{ nm})$  (adapted from Ref. 13).

of 11 planar layers of W,  $\text{TiO}_2$ , and  $\text{MgF}_2$  showed  $\bar{\alpha} > 0.94$  and  $\bar{\epsilon} < 0.07$ , as shown in Fig. 11(a). For 1750 K, the optimized structure composed of four layers of Mo and MgO showed  $\bar{\alpha} > 0.85$  and  $\bar{\epsilon} < 0.16$ .<sup>14</sup> They also calculated the performance of multilayer stacks deposited on V-groove gratings at 720 K. The V-groove provides an adiabatic transition from air to metal, thus yielding superior selectivity with fewer layers than required for the planar architecture. On the planar substrate, the 11 layers showed  $\bar{\alpha} = 0.95$  and  $\bar{\epsilon} = 0.06$ . The same selectivity is achieved with only five layers on the optimized V-groove grating, as shown in Fig. 11(b).<sup>15</sup>

Barshilia et al.<sup>16–18</sup> have investigated several combinations of multilayer selective solar absorbers. They optimized and fabricated a  $\text{Si}_3\text{N}_4(35 \text{ nm})/\text{NbAlON}(25 \text{ nm})/\text{NbAlN}(65$

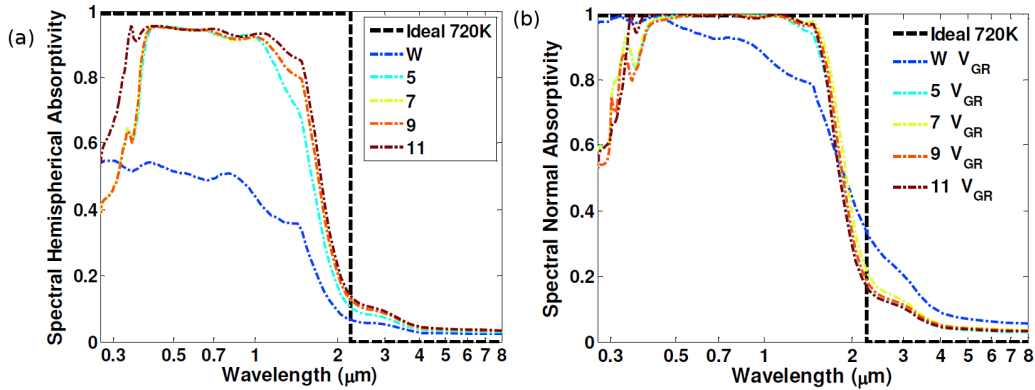


**FIG. 11:** (a) Simulated spectral absorptivity of optimized aperiodic metal dielectric stacks on a flat substrate using W,  $\text{TiO}_2$ , and  $\text{MgF}_2$  at 720 K (adapted from Ref. 14). (b) Simulated spectral absorptivity of optimized aperiodic metal dielectric stacks on the optimized Vgroove grating using W,  $\text{TiO}_2$ , and  $\text{MgF}_2$  at 720 K (adapted from Ref. 15).

nm) multilayer absorber on a copper substrate. This selective absorber showed  $\bar{\alpha} = 0.959$  and  $\bar{\epsilon} = 0.07$  (measured at 82°C). The  $\text{Si}_3\text{N}_4$  layer is an AR coating and the multilayer stack acts as a visible light absorber and IR reflector. The NbAlN layer has a higher metal volume fraction than NbAlON layer. By grading (decreasing) the refractive index from the substrate to the surface, reflection was reduced and solar absorptance was increased. After a heat treatment in air at 500°C for 2 h, its spectrally averaged absorptivity  $\bar{\alpha} = 0.943$  and emissivity  $\bar{\epsilon} = 0.10$  at 82°C. This structure was also found to be stable in air up to 350 h at 250°C.<sup>16</sup> They also optimized the AlON(92 nm)/TiAlN(62 nm) multilayer absorber with  $\bar{\alpha} = 0.93\text{--}0.942$  and  $\bar{\epsilon} = 0.05\text{--}0.06$ . After heat treatment in air at 600°C for 2 h, it exhibited high selectivity of  $\bar{\alpha} = 0.946$  and  $\bar{\epsilon} = 0.07$  at 82°C, but the solar selectivity significantly decreased at 625°C. The structure was stable up to 100 h at 400°C with  $\bar{\alpha} = 0.919$  and  $\bar{\epsilon} = 0.06$ .<sup>17</sup> In 2009, they optimized an  $\text{Al}_x\text{O}_y/\text{Al}/\text{Al}_x\text{O}_y$  tandem structure with  $\bar{\alpha} = 0.95\text{--}0.97$  and  $\bar{\epsilon} = 0.05\text{--}0.08$  at 82°C. The top  $\text{Al}_x\text{O}_y$  layer reduced visible light reflectance and the middle Al layer reflected IR radiation. After heat treatment in air at 400°C for 2 h, it exhibited solar selectivity of  $\bar{\alpha} = 0.901$  and  $\bar{\epsilon} = 0.06$  at 82°C, but the selectivity significantly degraded above 450°C. The structure was stable up to 75 h at 300°C.<sup>18</sup>

### 3.4 Cermets

Ceramic–metal composite coatings, also known as cermets, consist of nanoscale metal particles embedded in a ceramic matrix. A cermet selective solar absorber consists of an AR layer, one or more cermet layer(s), and a reflective substrate. The cermet acts as the primary absorber, while the reflective substrate, usually made from the same metal used in the cermet layer(s), helps to minimize absorption of undesired IR wavelengths. Cermet designs have a high degree of flexibility. Their solar selectivity can be optimized by varying metal and ceramic constituent elements, nanoparticle coating materials and thickness, as well as nanoparticle concentration, shape, size, and orientation.<sup>5</sup> Good candidates for the cermet constituents are metals with high melting points such as Cu, Au, Ni, Mo, Cr, Co, Pt, and W, and dielectrics such as oxides of the preceding compounds, along with  $\text{SiO}_2$ ,  $\text{Al}_2\text{O}_3$ , and  $\text{MgO}$ . Among these, the most widely used selective coatings, due to their low cost, are black chrome, a graded Cr–Cr<sub>2</sub>O<sub>3</sub> cermet,<sup>19–21</sup> and nickel-pigmented anodic  $\text{Al}_2\text{O}_3$ .<sup>22,23</sup> In another work, Sathiaraj et al.<sup>24</sup> optimized a single-layer cermet composed of Ni:Al<sub>2</sub>O<sub>3</sub> with homogeneous metal volume fraction of 0.61 on nickel-coated glass and experimentally measured  $\bar{\alpha} = 0.94$  and  $\bar{\epsilon} = 0.07$  at 100°C. It was stable up to 500°C in vacuum.<sup>24</sup>

Generally, a single homogeneous cermet film does not show extremely high solar selectivity by itself, since the absorption of the cermet causes an impedance mismatch with the AR coating. Thus, more complex structures with a more gradual change in absorption have also been investigated. A first candidate was a graded cermet whose metal concentration gradually decreased from the bottom of the film to the top.<sup>25</sup> A second possible structure was a double cermet that consisted of two layers of a low metal volume fraction layer deposited on a high metal volume fraction layer.<sup>26</sup> The schematic of these two structures depicted in Fig. 12 offers greater flexibility and potentially higher performance.

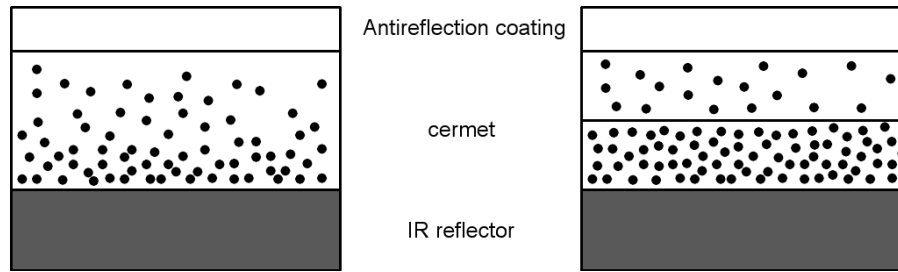


**FIG. 12:** Schematic of a cermet with a graded metal concentration (left) and a double cermet composed of low and high metal volume fraction layers (right).

Craighead et al.<sup>27</sup> co-evaporated Pt and  $\text{Al}_2\text{O}_3$  to form a graded composition-depth profile from 100% metal fraction at the bottom to 0% metal fraction at the top. Textured  $\text{SiO}_2$  was used for AR coating and Pt was used for the IR reflector. The optimized structure had a measured absorptivity of  $\bar{\alpha} = 0.98$  and emissivity of  $\bar{\epsilon} = 0.21\text{--}0.36$  at  $200^\circ\text{C}$ .<sup>27</sup> Lanxner and Elgat<sup>28</sup> developed a  $\text{Mo}:\text{Al}_2\text{O}_3$  cermet with a graded metal concentration ranging from 0 to 0.5. Their optimized structure was found to have an absorptivity of  $\bar{\alpha} = 0.96$  and emissivity of  $\bar{\epsilon} = 0.1$  at  $350^\circ\text{C}$ ; furthermore, no degradation of the coating was observed after heat treatment in vacuum at  $650^\circ\text{C}$  for one month.<sup>28</sup> Farooq et al.<sup>29</sup> made a  $\text{Ni}:\text{SiO}_2$  cermet with metal volume fractions varying from 0.1 to 0.9. It was observed to have an absorptivity of  $\bar{\alpha} = 0.90\text{--}0.96$  and emissivity of  $\bar{\epsilon} = 0.03\text{--}0.14$  at  $27^\circ\text{C}$ .<sup>29</sup> Zhang et al.<sup>30</sup> optimized several double cermet structures, in which the optimized  $\text{Mo}:\text{Al}_2\text{O}_3$  double cermet was composed of  $\text{Al}_2\text{O}_3/\text{Mo}:\text{Al}_2\text{O}_3(f = 0.34)/\text{Mo}:\text{Al}_2\text{O}_3(f = 0.53)/\text{Mo}$  on a Cu substrate and absorptance of 0.955 and normal emittance of 0.032 at room temperature and 0.08 at  $350^\circ\text{C}$  were obtained.<sup>30</sup> Stainless steel, nickel-based alloy  $\text{Ni}_{80}\text{Cr}_{20}$  (NiCr), molybdenum-based alloy  $\text{Mo}_{99}\text{Ti}_{0.5}\text{Zr}_{0.1}$ , and tungsten metals with an AlN dielectric host, AlN AR coating, and Al back reflector were tested experimentally. For all of these metal:AlN double cermet designs, solar absorptance of 0.92–0.96 and a normal emittance of 0.03–0.05 were measured at room temperature, and a normal emittance of 0.07–0.10 at  $350^\circ\text{C}$  was measured.<sup>31</sup> Furthermore, Al:AlON cermet coatings were also numerically simulated and fabricated. Structures consisting of the following layers—AlN/Al:AlON( $f = 0.143$ )/Al:AlON( $f = 0.275$ )/Al—showed a solar absorptance of 0.96 and emittance of 0.08 at  $80^\circ\text{C}$ .<sup>32</sup> Another Al:AlON cermet with the following structure— $\text{Al}_2\text{O}_3/\text{Al:AlON}(f = 0.093)/\text{Al:AlON}(f = 0.255)/\text{Al}$ —displayed very strong performance, with absorptivity of  $\bar{\alpha} = 0.974$  and emissivity of  $\bar{\epsilon} = 0.033$  at  $80^\circ\text{C}$ .<sup>33</sup> Recently, Chester et al.<sup>34</sup> optimized four-layer cermet structures with W and  $\text{SiO}_2$  for two sets of operating conditions. For unconcentrated sunlight ( $C = 1$ ) at an absorber temperature  $T = 400$  K, four layers of  $\text{W}:\text{SiO}_2$  with increasing metal volume fraction showed  $\bar{\alpha} = 0.979$  and  $\bar{\epsilon} = 0.042$  at 400 K for a thermal transfer efficiency of 0.843. For concentrated sunlight ( $C = 100$ ) at an absorber temperature  $T = 1000$  K, the optimized design showed  $\bar{\alpha} = 0.945$  and  $\bar{\epsilon} = 0.172$  at 1000 K for a thermal transfer efficiency of 0.7559. The overall performance of this optimized four-layer structure exceeds that of any other cermet-based selective solar absorber found in the literature with 100 sun concentration operating at 1000 K.<sup>34</sup> By comparison, measurements on premium cermet-based selective solar absorbers

available commercially from companies such as Almeco-TiNOX and Alanod Solar correspond to absorptivity of  $\bar{\alpha} = 0.95$  and emissivity of  $\bar{\epsilon} = 0.04\text{--}0.05$  at  $20^\circ\text{C}$ .<sup>34</sup> Thus, the performance of commercial selective solar absorbers will come in somewhat lower than the previously presented multilayer cermet designs at realistic operating temperatures.

### 3.5 Surface Texturing

Surface texturing is a common approach to increase solar absorptivity, which functions by generating multiple internal reflections. An ideally roughened surface simultaneously displays high absorptivity at short wavelengths and low emissivity at longer wavelengths. Dendrite or porous microstructures with feature sizes comparable to the wavelengths of incident solar radiation can be useful in tailoring the optical properties of solar absorbers. Short-wavelength photons are easily trapped inside the surface, as shown in Fig. 13(a). On the other hand, photons with wavelengths larger than the dendrite spacing see a flat surface.<sup>6</sup>

Ideally, surface-textured absorbers display several other features. For example, the morphology of the textured surface should withstand high temperature, and it must be protected from external damages such as contact or abrasion by protective coatings like sol-gels. Some polymer protection coatings may limit the working temperature range; therefore, selecting coating materials suitable to high-temperature application is important. Selection of surface materials with high absorptivity will further increase the overall efficiency.<sup>5</sup>

There are several ways to create surface texturing including: (1) unidirectional solidification of eutectic alloys; (2) x-ray, e-beam, or nanoimprint lithography; (3) ion-exchange reactions between metals; (4) vapor–liquid–solid mechanism; (5) vapor deposition; and (6) oxidation of metals at high temperature. A more-detailed explanation can be found in Ref. 5. Kussmaul et al.<sup>35</sup> textured a copper surface with an ion beam [Fig. 13(b)], which resulted in high values of thermal emittance of 0.978 and 0.983 at 700 and 900 K, respectively.<sup>35</sup>

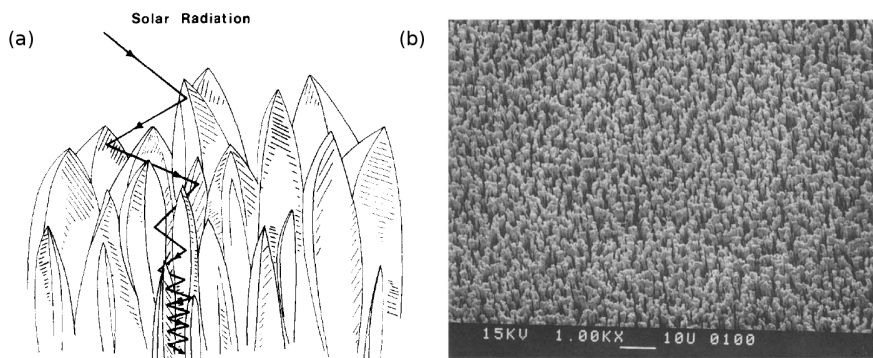


**FIG. 13:** (a) Schematic representation of a dendritic selective surface. Incoming sunlight can be internally reflected up to 50 times to enhance absorption (adapted from Ref. 6). (b) SEM image of copper textured via an ion beam (adapted from Ref. 35).

Nanowire growth on a flat surface can also give rise to high-quality texturing that dramatically increases short-wavelength absorption.<sup>36</sup> Recently, Zhu et al.<sup>37</sup> grew amorphous silicon ( $\alpha$ -Si) nanowires and nanocones through a simple chlorine reactive ion etching process. Particularly strong enhancement in absorption was shown for  $\alpha$ -Si nanocones over a large range of angles of incidence and wavelengths. The scanning electron microscope (SEM) image of the nanocones is shown in Fig. 14(a). The sample looked dark due to its high absorptivity in the visible range, as shown in Fig. 14(b). The measured absorptance of the nanocone sample maintained 0.93 in the visible range at normal incidence, as shown in Fig. 14(c). This enhancement is explained by superior impedance matching between  $\alpha$ -Si and air through a gradual reduction of the effective refractive index, resulting in excellent antireflection properties.<sup>37</sup>

### 3.6 Photonic Crystals

According to Planck's law of blackbody radiation, the thermal radiation spectrum of all emitter structures is proportional to their photon density of states. PhCs provide an unprecedented ability to control the photon density of states in a wide range of systems including, but not limited to, selective solar absorbers. PhCs are made from periodic arrangements of two or more materials with distinct dielectric constants, which can give rise to a complete photonic band gap—a range of wavelengths that are completely reflected for all incident angles and polarizations. In the context of selective solar absorbers, photonic band gaps can wholly suppress emission over a range of wavelengths that can be chosen to correspond to the optimum reflectivity calculated; e.g., in Fig. 1. Furthermore, 2D and 3D structures can give rise to strongly angle-dependent photon densities of states; this implies that emission in directions pointed away from the sun can be strongly suppressed in order to increase thermal transfer efficiencies even beyond the limits calculated in Fig. 3.

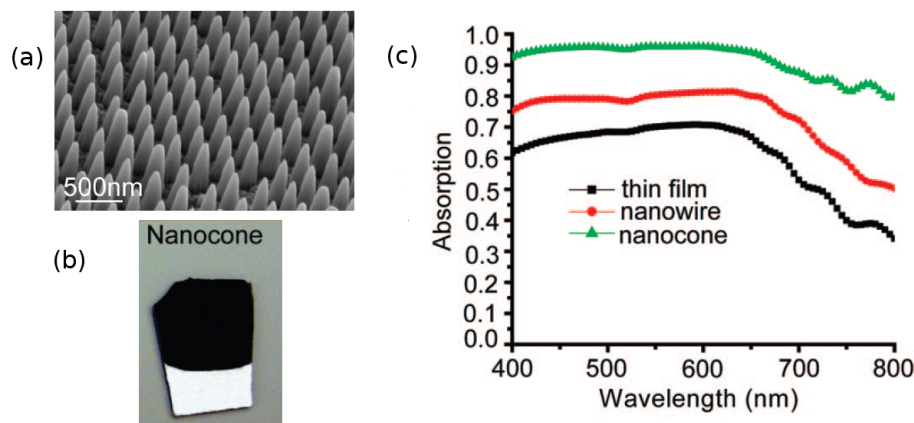


**FIG. 14:** (a) SEM images of  $\alpha$ -Si nanocones; (b) photographs of  $\alpha$ -Si nanocone arrays; (c) measured absorption on samples with  $\alpha$ -Si thin film,  $\alpha$ -Si nanowires, and  $\alpha$ -Si nanocones (adapted from Ref. 37).

### 3.6.1 One-Dimensional Photonic Crystals

One-dimensional (1D) patterns, or gratings, on the surface of a material strongly impact the optical properties of the bulk material. This is attributed to surface plasmon and standing wave resonance by the surface gratings. The effects of the geometry of gratings such as periodicity and depth on spectral behavior have been studied.<sup>38,39</sup> Recently, Chen et al.<sup>40,41</sup> proposed a 1D tungsten complex grating design. The complex grating is defined by the superposition of two or more 1D grating profiles. The complex design provides better sharpness and angle dependence of the emittance peak than that of simple 1D gratings. The schematic of the complex grating and its simulated emittance curve are shown in Fig. 15. The peak value is higher than 0.8 between  $\lambda = 0.8$  and  $1.6 \mu\text{m}$  and lower than 0.2 above  $\lambda = 2.2 \mu\text{m}$ .<sup>40</sup>

### 3.6.2 Two-Dimensional Photonic Crystals

Heinzel et al.<sup>42</sup> fabricated 2D tungsten PhCs with a square array of cylindrical holes. The emissivity of the tungsten increased from 0.3 to 0.7 at  $\lambda = 1.6 \mu\text{m}$  by the coupling of surface plasmons to electromagnetic radiation.<sup>42</sup> Sai and co-workers<sup>43–45</sup> developed 2D deep gratings with rectangular microcavities. The emittance was greater than 0.8 for  $\lambda = 0.5–1.8 \mu\text{m}$ , and below 0.2 for  $\lambda > 2.1 \mu\text{m}$  at normal incidence.<sup>46</sup> Celanovic et al.<sup>47</sup> fabricated 2D W PhCs with a square array of deep cylindrical holes. Spontaneous thermal emission spectra were measured for several designs with different hole radii and depths. Large emittance enhancement was observed below the cutoff wavelength of  $\lambda = 1.7 \mu\text{m}$ , as shown in Fig. 16(a)<sup>47</sup>. They also explored the 2D hexagonal pattern of air holes in a W substrate. Numerical simulations indicated a complete band gap was present, resulting in suppressed emission for wavelengths greater than  $1.8 \mu\text{m}$ , as shown in Fig. 16(b).<sup>48</sup>

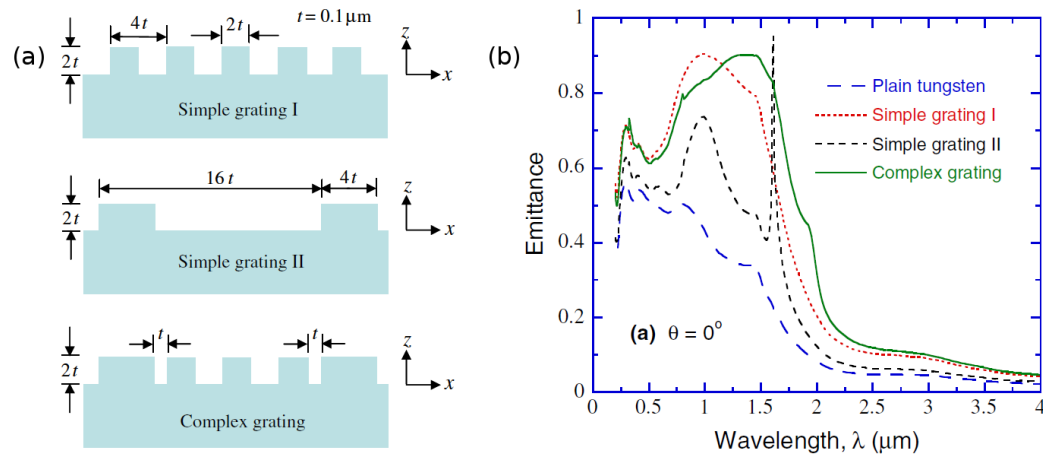


**FIG. 15:** (a) Three tungsten grating designs: two relatively simple designs and one complex grating formed from superimposing both on top of each other. (b) Simulated emittance of the complex grating of the two simple tungsten gratings shown in (a) at normal incidence (adapted from Ref. 41).

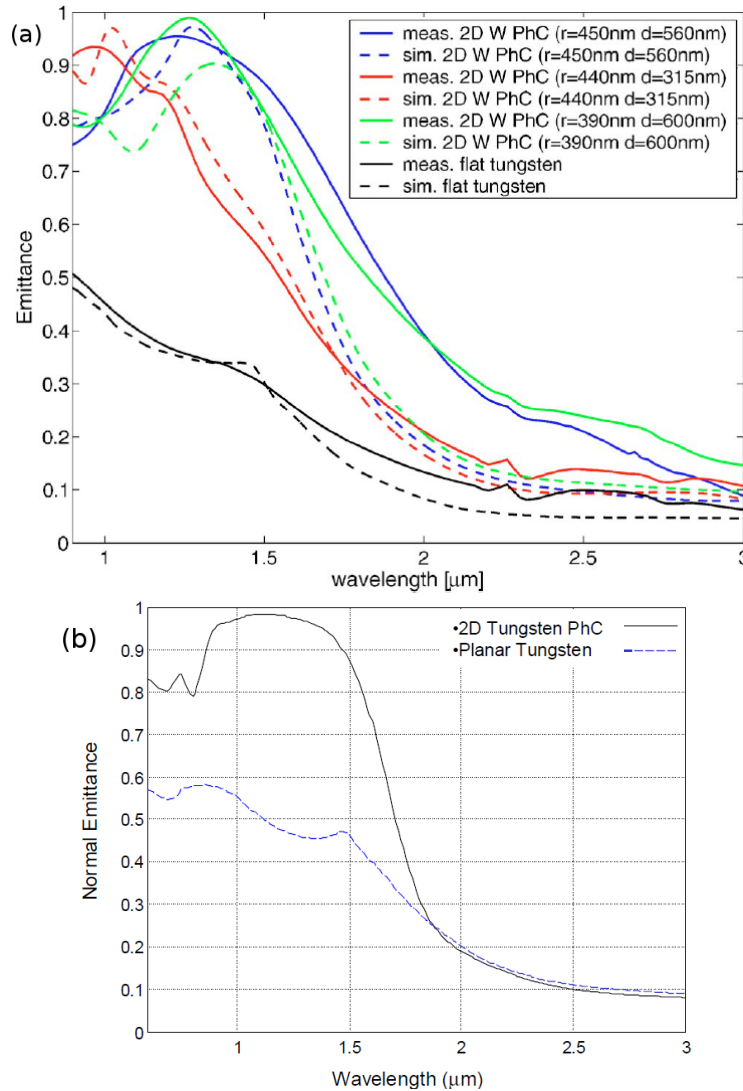


**FIG. 16:** (a) Measured (dot) and simulated (solid) emittance for a flat tungsten and three 2D W PhCs composed of a square array of air holes (adapted from Ref. 47). (b) Simulated normal emittance curves of a 2D W PhC composed of a hexagonal array of air holes (adapted from Ref. 48).

Rephaeli and Fan<sup>49,50</sup> designed 2D W PhCs with a square array of pyramids, as shown in Fig. 17(a). The pyramidal shape provided an impedance matching between the free space and tungsten, which lowered the surface reflection, enabling light to be efficiently absorbed. Absorptivity was close to 1 for  $\lambda < 2 \mu\text{m}$  for several variations of this design, as shown in Fig. 17(b).<sup>49,50</sup>

Recently, Wang et al.<sup>51</sup> proposed 2D Mo PhCs with a square array of microcones. Similar to tungsten, molybdenum is also stable at high temperature and shows superior



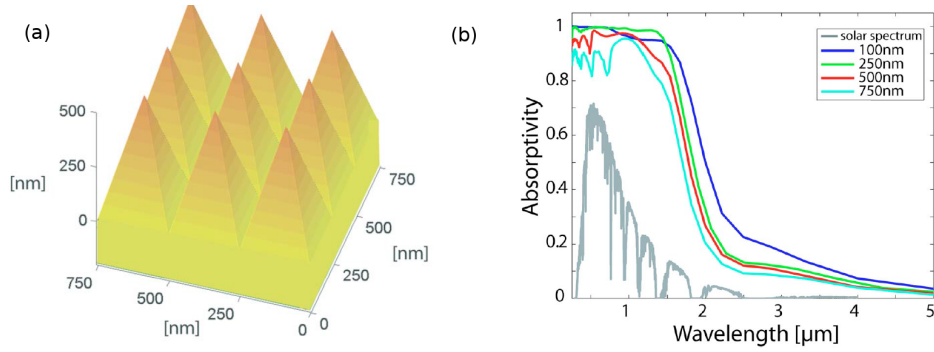


**FIG. 17:** (a) Illustration of a tungsten pyramid PhC. (b) Simulated absorptivity of (a) with different periods (adapted from Ref. 49).

intrinsic solar selectivity. In Fig. 18, a schematic diagram of the Mo PhC and its normal reflectance curves with different aspect ratios are shown. The optimized microcone Mo PhC surface exhibited  $\bar{\alpha} = 0.919$  and  $\bar{\epsilon} = 0.149$  at  $1000^\circ\text{C}$ , showing its potential for high-temperature applications.<sup>51</sup>

Work performed by Chang and colleagues<sup>52</sup> has experimentally shown that cone-shaped silicon 2D PhCs can offer extremely low reflectivities for a broad range of visible light wavelengths. Fig. 19 shows reflectivity over all angles and polarizations to be 0.01, implying extremely high values of  $\bar{\alpha}$ . Placing a reflector in back should also lead to low  $\bar{\epsilon}$  values in the IR, since silicon will only display free carrier absorption there. Future work will determine the exact values of  $\bar{\alpha}$  and  $\bar{\epsilon}$  for this structure in selective absorber applications.

### 3.6.3 Three-Dimensional Photonic Crystals

Efforts by Lin et al.<sup>53</sup> on 3D woodpile structures have shown the potential for strong spectral selectivity characteristics to be achieved with a relatively modest number of layers.

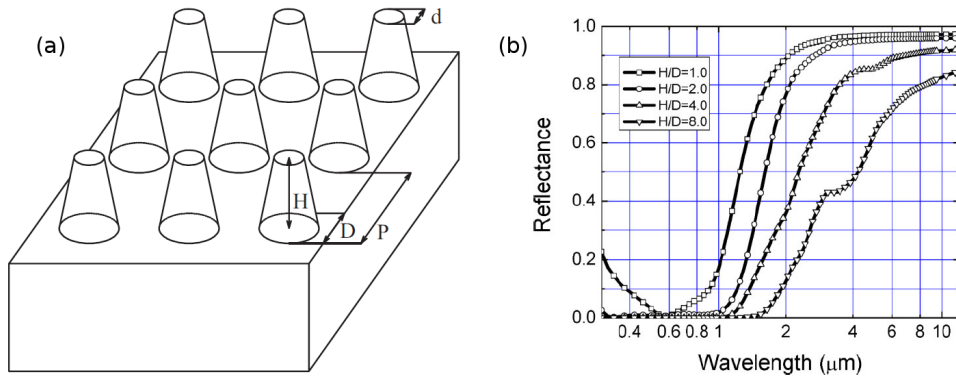


**FIG. 18:** (a) Schematic diagram of a microcone PhC. (b) Simulated reflectance spectrum of microcone PhCs with different aspect ratios (adapted from Ref. 51).

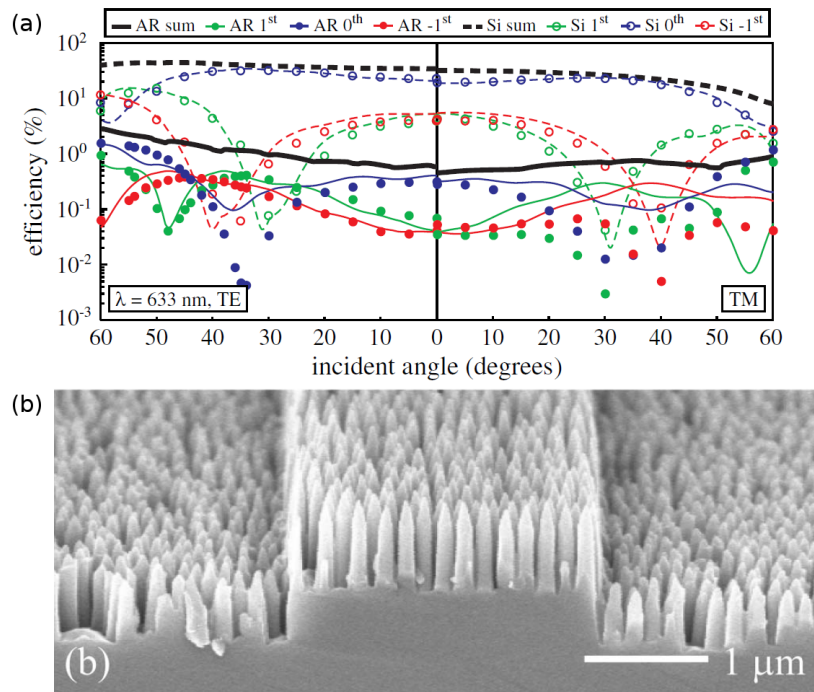


**FIG. 19:** (a) Selective absorber reflectivity for all angles and polarizations of a silicon 2D PhC at 633 nm; circles represent experimental data and lines represent simulations. (b) SEM image showing the structure as fabricated (adapted from Ref. 52).

In particular, they were able to show both with numerical simulations [Fig. 20(a)] as well as experiments [Fig. 20(b)] that absorptivity of about 0.3 up to the cutoff wavelength can be achieved at normal incidence, along with extremely low emissivity of 0.02 for both mid-wavelength and long-wavelength IR.<sup>53</sup> In order to make this approach suitable for selective solar absorbers, additional work would be needed to boost the spectrally averaged

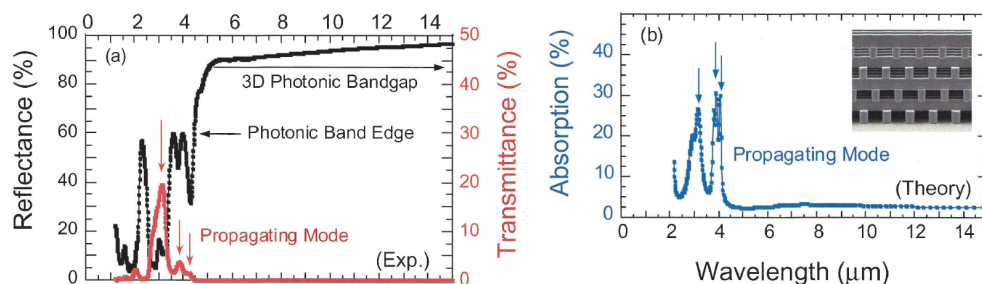


**FIG. 20:** Theoretical calculations of the reflectance and transmittance of an eight-layer woodpile 3D PhC (the  $x$  axis is the wavelength in microns). (b) Experimentally measured absorptivity spectrum of a 3D PhC, with an inset illustrating the fabricated structure (adapted from Ref. 53).

absorptivity as close to that of a blackbody as possible for short wavelengths, while not increasing the long-wavelength emissivity more than a proportional amount. Nonetheless, in principle, this approach may be the most promising for extremely high performance, particularly at high temperatures.

#### 4. SUMMARY

Selective solar absorbers are a critical technology necessary for effectively capturing sunlight as heat. We have defined an appropriate figure of merit to measure their performance; i.e., the thermal transfer efficiency. Within this general technological framework, there are six major designs: intrinsic absorbers, semiconductor–metal tandems, multilayer stacks, cermet, absorbers with surface texturing, and PhC-based designs. The results for specific examples within each class are summarized in Table 1. We found that the highest performance designs built and tested to date are multilayer ceramic and metal nanocom-

**TABLE 1:** Selective solar absorbers

Type	Material	Experiment			Simulation			Thermal stability (°C)
		$\alpha$	$\varepsilon$	Measurement temperature (°C)	$\alpha$	$\varepsilon$	Measurement temperature (°C)	
Intrinsic	Si <sub>3</sub> N <sub>4</sub> /ZrB <sub>2</sub> (Ref. 7)	0.93	0.09	102				527
Semiconductor/metal	ARC*/Si/Ge/Ag (Ref. 8)				0.89	0.0389	300	
					0.89	0.0545	500	
	SiO <sub>2</sub> /TiO <sub>2</sub> /α-Si/Al (Ref. 9)	0.79–0.81	0.12–0.14	400				400
	4 FCs** + Ge + 1 BC*** + Ag (Ref. 4)				0.907	0.016	127	
	4 FCs + Si + 1 BC + Ag (Ref. 4)				0.868	0.073	727	
Multi-layer	SiO <sub>2</sub> /Ti/SiO <sub>2</sub> /Al (Ref. 13)	0.95	0.063	327				
	11 layers of W, TiO <sub>2</sub> , and MgF <sub>2</sub> (Ref. 14)				>0.95	<0.06	447	
	4 layers of Mo and MgO (Ref. 14)				>0.85	<0.16	1477	
	11 layers of W, TiO <sub>2</sub> , and MgF <sub>2</sub> on the V groove (Ref. 15)				0.95	0.06	447	
	Si <sub>3</sub> N <sub>4</sub> /NbAlON/NbAlN (Ref. 16)	0.959	0.07	82				250
	AlON/TiAlN (Ref. 17)	0.93–0.942	0.05–0.06	82				400
	Al <sub>x</sub> O <sub>y</sub> /Al/Al <sub>x</sub> O <sub>y</sub> (Ref. 18)	0.95–0.97	0.05–0.08	82				300

TABLE 1: Continued

Type	Material	Experiment			Simulation			Thermal stability (°C)
		$\alpha$	$\varepsilon$	Measurement temperature (°C)	$\alpha$	$\varepsilon$	Measurement temperature (°C)	
Cermet	SiO <sub>2</sub> /Ni:Al <sub>2</sub> O <sub>3</sub> ( $f = 0.61$ )/Ni (Ref. 24)	0.94	0.07	100				500
	SiO <sub>2</sub> (textured)/Pt:Al <sub>2</sub> O <sub>3</sub> ( $f = 0 \rightarrow 1$ )/Pt (Ref. 27)	0.98	0.21–0.36	200				
	SiO <sub>2</sub> /Mo:Al <sub>2</sub> O <sub>3</sub> ( $f = 0 \rightarrow 0.5$ )/Mo (Ref. 28)	0.96	0.1	350				650
	SiO <sub>2</sub> /Ni:SiO <sub>2</sub> ( $f = 0.1 \rightarrow 0.9$ )/Ni (Ref. 29)	0.90–0.96	0.03–0.14					
	Al <sub>2</sub> O <sub>3</sub> /Mo:Al <sub>2</sub> O <sub>3</sub> ( $f = 0.34$ )/Mo:Al <sub>2</sub> O <sub>3</sub> ( $f = 0.53$ )/Mo (Ref. 30)	0.955	0.032	23				
		0.955	0.08	350				
	AlN/Al:AlON ( $f = 0.143$ )/Al:AlON ( $f = 0.275$ )/Al (Ref. 32)	0.96	0.08	80	0.958	0.035	80	400
	Al <sub>2</sub> O <sub>3</sub> /Al:AlON ( $f = 0.093$ )/Al:AlON ( $f = 0.255$ )/Al (Ref. 33)				0.974	0.033	80	
	FC + 4 layers of W:SiO <sub>2</sub> + Reflector (Ref. 34)				0.979	0.042	127	
Surface texture					0.945	0.172	727	
	Cu surface texture (Ref. 35)	0.978		427				
		0.983		627				
PhC	$\alpha$ -Si nanocones (Ref. 37)	>0.93						
	1D complex gratings (Ref. 40)				>0.8	<0.2		
	2D W square array rectangular air holes (Ref. 46)	>0.8	<0.2					
	2D W square array cylindrical air holes (Ref. 47)	>0.8	<0.1					
	2D W hexagonal array cylindrical air holes (Ref. 48)				>0.95	<0.1		
	2D W square array pyramids (Ref. 49)				>0.99	<0.1		
	2D Mo square array microcones (Ref. 51)				0.919	0.149	1000	

\* ARC: anti-reflection coating

\*\* FC: front coating

\*\*\* BC: back coating

posites, known as cermets. Furthermore, several research papers over the last few years have suggested even further improvements are possible with carefully designed multilayer cermets. Nonetheless, PhC-based designs offer great promise for future high-performance designs. Not only can PhCs offer unprecedented control over thermal emission as a function of wavelength, but they can also offer unique control over emission as a function of angle, opening up the possibility of only exchanging heat with the sun, in order to achieve high-temperature operation even without optical concentration. The potential for high performance at high temperatures is particularly important, since the highest theoretical efficiency for conversion of heat into electricity is at high operating temperatures (for a fixed cold-side temperature).

## ACKNOWLEDGMENTS

We thank Yi Xiang Yeng for valuable discussions. This work was supported in part by the MRSEC Program of the National Science Foundation under Award No. DMR-0819762 (P.B.), the MIT S3TEC Energy Research Frontier Center of the Department of Energy under Grant No. DE-SC0001299 (J.L.), and the Army Research Office through the Institute for Soldier Nanotechnologies (I.C.) under Contract Nos. DAAD-19-02-D0002 and W911NF-07-D0004.

## REFERENCES

1. R. B. Ram Gupta, ed., *Hydrogen Fuel: Production, Transportation, and Storage*, Boca Raton, FL: CRC, 2009.
2. B. D. Wedlock, Thermo-photo-voltaic energy conversion, *Proc. IEEE*, **51**:694–698, 1963.
3. R. E. Black, P. F. Baldasaro, and G. W. Charache, Thermophotovoltaics-development status and parametric considerations for power applications, *Proc. of 18th International Conference on Thermoelectrics*, **18**:639–644, 1999.
4. P. Bermel, M. Ghebrebrhan, W. Chan, Y. X. Yeng, M. Araghchini, R. Hamam, C. H. Marton, K. F. Jensen, M. Soljacic, J. D. Joannopoulos, S. G. Johnson, and I. Celanovic, Design and global optimization of high-efficiency thermophotovoltaic systems, *Opt. Express*, **18**:A314–A334, 2010.
5. C. E. Kennedy, Review of mid- to high temperature solar selective absorber materials, *Report*, Golden, CO: National Renewable Energy Laboratory Research, 2002.
6. C. M. Lampert, Coatings for enhanced photothermal energy collection. I: Selective absorbers, *Sol. Energy Mater.*, **1**:319–341, 1979.
7. E. Randich and D. D. Allred, Chemically vapor-deposited  $ZrB_2$  as a selective solar absorber, *Thin Solid Films*, **83**:393–398, 1981.
8. A. Donnadiou and B. O. Seraphin, Optical performance of absorber–reflector combinations for photothermal solar energy conversion, *J. Opt. Soc. Am.*, **68**:292–297, 1978.
9. M. Okuyama, K. Saji, T. Adachi, H. Okamoto, and Y. Hamakawa, Selective absorber using glow-discharge amorphous silicon for solar photothermal conversion, *Sol. Energy Mater.*, **3**:405–413, 1980.

10. A. Narayanaswamy and G. Chen, Thermal emission control with one-dimensional metallodielectric photonic crystals, *Phys. Rev. B*, **70**:125101-1–125101-4, 2004.
11. A. Narayanaswamy, J. Cybulski, and G. Chen, 1D Metallo-dielectric photonic crystals as selective emitters for thermophotovoltaic applications, *AIP Conf. Proc.*, **738**:215–220, 2004.
12. S. Y. Lin, J. Moreno, and J. G. Fleming, Three-dimensional photonic-crystal emitter for thermal photovoltaic power generation, *Appl. Phys. Lett.*, **83**:380–382, 2003.
13. X. Li, Y. Chen, J. Miao, P. Zhou, Y. Zheng, L. Chen, and Y. Lee, High solar absorption of a multilayered thin film structure, *Opt. Express*, **15**:1907–1912, 2007.
14. N. P. Sergeant, O. Pincon, M. Agrawal, and P. Peumans, Design of wide-angle solar-selective absorbers using aperiodic metal-dielectric stacks, *Opt. Express*, **17**:22800–22812, 2009.
15. N. P. Sergeant, M. Agrawal, and P. Peumans, High performance solar-selective absorbers using coated sub-wavelength gratings, *Opt. Express*, **18**:5525–5540, 2010.
16. H. C. Barshilia, N. Selvakumar, K. S. Rajam, and A. Biswas, Spectrally selective NbAlN/NbAlON/Si<sub>3</sub>N<sub>4</sub> tandem absorber for high-temperature solar applications, *Sol. Energy Mater. Sol. Cells*, **92**:495–504, 2008.
17. H. C. Barshilia, N. Selvakumar, K. S. Rajam, and A. Biswas, Optical properties and thermal stability of TiAlN/AlON tandem absorber prepared by reactive DC/RF magnetron sputtering, *Sol. Energy Mater. Sol. Cells*, **92**:1425–1433, 2008.
18. H. C. Barshilia, N. Selvakumar, G. Vignesh, K. S. Rajam, and A. Biswas, Optical properties and thermal stability of pulsed-sputter-deposited Al<sub>x</sub>O<sub>y</sub>/Al/Al<sub>x</sub>O<sub>y</sub> multilayer absorber coatings, *Sol. Energy Mater. Sol. Cells*, **92**:315–323, 2009.
19. G. E. McDonald, Spectral reflectance properties of black chrome for use as a solar selective coating, *Sol. Energy*, **17**:119–122, 1975.
20. J. C. C. Fan and S. A. Spura, Selective black absorbers using rf-sputtered Cr<sub>2</sub>O<sub>3</sub>/Cr cermet films, *Appl. Phys. Lett.*, **30**:511–513, 1977.
21. C. M. Lampert and J. Washburn, Microstructure of a black chrome solar selective absorber, *Sol. Energy Mater.*, **1**:81–92, 1979.
22. A. Andersson, O. Hunderi, and C. G. Granqvist, Nickel pigmented anodic aluminum oxide for selective absorption of solar energy, *J. Appl. Phys.*, **51**:754–764, 1980.
23. A. Scherer, O. T. Inal, and R. B. Pettit, Modelling of degradation of nickel-pigmented aluminium oxide photothermal collector coatings, *J. Mater. Sci.*, **23**:1934–1942, 1988.
24. T. S. Sathiaraj, R. Thangaraj, H. Al Sharbaty, M. Bhatnagar, and O. P. Agnihotri, Ni:Al<sub>2</sub>O<sub>3</sub> selective cermet coatings for photothermal conversion up to 500°C, *Thin Solid Films*, **190**:241–254, 1989.
25. B. Window, D. McKenzie, and G. Harding, Selective absorber design, *Sol. Energy Mater.*, **2**:395–401, 1980.
26. I. T. Ritchie and B. Window, Applications of thin graded-index films to solar absorbers, *Appl. Opt.*, **16**:1438–1443, 1977.
27. H. G. Craighead, R. E. Howard, J. E. Sweeney, and R. A. Buhrman, Graded-index Pt-Al<sub>2</sub>O<sub>3</sub> composite solar absorbers, *Appl. Phys. Lett.*, **39**:29–31, 1989.
28. M. Lanxner, and Z. Elgat, Solar selective absorber coatings for high service temperatures, produced by plasma sputtering, *Proc. SPIE*, **1272**:240–249, 1990.
29. M. Farooq, A. A. Green, and M. G. Hutchins, High performance sputtered Ni:SiO<sub>2</sub> composite

- solar absorber surfaces, *Sol. Energy Mater. Sol. Cells*, **54**:67–73, 1998.
30. Q. Zhang, Y. Yin, and D. R. Mills, High efficiency Mo:Al<sub>2</sub>O<sub>3</sub> cermet selective surfaces for high-temperature application, *Sol. Energy Mater. Sol. Cells*, **40**:43–53, 1996.
  31. Q. Zhang, Metal–AlN cermet solar selective coatings deposited by direct current magnetron sputtering technology, *J. Phys. D*, **31**:355–362, 1998.
  32. Q.-C. Zhang, K. Zhao, B.-C. Zhang, L.-F. Wang, Z.-L. Shen, D.-Q. Lu, D.-L. Xie, and B.-F. Li, High performance Al–N cermet solar coatings deposited by a cylindrical direct current magnetron sputter coater, *J. Vac. Sci. Technol. A*, **17**:2885–2890, 1999.
  33. Q. Zhang, High efficiency Al–N cermet solar coatings with double cermet layer film structures, *J. Phys. D*, **32**:1938–1944, 1999.
  34. D. Chester, P. Bermel, J. D. Joannopoulos, M. Soljacic, and I. Celanovic, Design and global optimization of high-efficiency solar thermal systems with tungsten cermets, *Opt. Express*, **19**:A245–A257, 2011.
  35. M. Kussmaul, M. J. Mirtich, and A. Curren, Ion beam treatment of potential space materials at the NASA Lewis Research Center, *Surf. Coat. Technol.*, **51**:299–306, 1992.
  36. M. H. Huang, S. Mao, H. Feick, H. Yan, Y. Wu, H. Kind, E. Weber, R. Russo, and P. Yang, Room-temperature ultraviolet nanowire nanolasers, *Science*, **292**:1897–1899, 2001.
  37. J. Zhu, Z. Yu, G. F. Burkhard, C. Hsu, S. T. Connor, Y. Xu, Q. Wang, M. McGehee, S. Fan, and Y. Cui, Optical absorption enhancement in amorphous silicon nanowire and nanocone arrays, *Nano Lett.*, **9**:279–282, 2009.
  38. H. Sai, Y. Kanamori, K. Hane, and H. Yugami, Numerical study on spectral properties of tungsten one-dimensional surface-relief gratings for spectrally selective devices, *J. Opt. Soc. Am. A*, **22**:1805–1813, 2005.
  39. J. T. K. Wan, Tunable thermal emission at infrared frequencies via tungsten gratings, *Opt. Commun.*, **282**:1671–1675, 2009.
  40. Y. Chen and Z. M. Zhang, Design of tungsten complex gratings for thermophotovoltaic radiators, *Opt. Commun.*, **269**:411–417, 2007.
  41. B. Chen, D. Yang, P. A. Charpentier, and S. Nikumb, Optical and structural properties of pulsed laser deposited Ti:Al<sub>2</sub>O<sub>3</sub> thin films, *Sol. Energy Mater. Sol. Cells*, **92**:1025–1029, 2008.
  42. A. Heinzl, V. Boerner, A. Gombert, B. Bläsi, V. Wittwer, and J. Luther, Radiation filters and emitters for the NIR based on periodically structured metal surfaces, *J. Mod. Opt.*, **47**:2399–2419, 2000.
  43. H. Sai, H. Yugami, Y. Kanamori, and K. Hane, Solar selective absorbers based on two-dimensional W surface gratings with submicron periods for high-temperature photothermal conversion, *Sol. Energy Mater. Sol. Cells*, **79**:35–49, 2003.
  44. H. Sai, Y. Kanamori, and H. Yugami, High-temperature resistive surface grating for spectral control of thermal radiation, *Appl. Phys. Lett.*, **82**:1685–1687, 2003.
  45. H. Sai and H. Yugami, Thermophotovoltaic generation with selective radiators based on tungsten surface gratings, *Appl. Phys. Lett.*, **85**:3399–3401, 2004.
  46. H. Sai, Y. Kanamori, and H. Yugami, Tuning of the thermal radiation spectrum in the near-infrared region by metallic surface microstructures, *J. Micromech. Microeng.*, **15**:S243–S249, 2005.
  47. I. Celanovic, N. Jovanovic, and J. Kassakian, Two-dimensional tungsten photonic crystals as

- selective thermal emitters, *Appl. Phys. Lett.*, **92**:193101-1–193101-3, 2008.
48. I. Celanovic, F. O'Sullivan, N. Jovanovic, M. Qi, and J. G. Kassakian, 1D and 2D photonic crystals for thermophotovoltaic applications, *Proc. SPIE*, **5450**:416–422, 2004.
  49. E. Rephaeli and S. Fan, Tungsten black absorber for solar light with wide angular operation range, *Appl. Phys. Lett.*, **92**:211107-1–211107-3, 2008.
  50. E. Rephaeli and S. Fan, Absorber and emitter for solar thermo-photovoltaic systems to achieve efficiency exceeding the Shockley–Queisser limit, *Opt. Express*, **17**:15145–15159, 2009.
  51. J. Wang, Z. Chen, and D. Li, Simulation of two-dimensional Mo photonic crystal surface for high-temperature solar-selective absorber, *Phys. Status Solidi A*, **207**:1988–1992, 2010.
  52. C.-H. Chang, J. A. Dominguez-Caballero, H. J. Choi, and G. Barbastathis, Nanostructured gradient-index antireflection diffractive optics, *Opt. Lett.*, **36**:2354–2356, 2011.
  53. S.-Y. Lin, J. G. Fleming, and I. El-Kady, Three-dimensional photonic-crystal emission through thermal excitation. *Opt. Lett.*, **28**:1909–1911, 2003.